## Supplementary Information

Catalyst evaluation. The catalytic performance of as-synthesized samples was evaluated *via* a 50 mL Hastelloy Alloy reactor. In a typical reaction, 20 mg catalysts were suspended in 20 mL distilled water in the reactor. Gases with a fixed pressure of 28 bar (20 bar CH_4, 3 bar O_2, and 5 bar CO) were injected into the reaction system. The reaction temperature change from 100 to 170 °C and the reaction time from 5min to 1h.

Determination of the liquid phase products was conducted on a Bruker JNM-ECZ600R/S1 600 MHz NMR instrument. Generally, 0.3 mL of D_2O was mixed with 0.7 mL of the sample solution inside an NMR tube. Oxygenates identified by 1H NMR include CH_3OH ($\delta = 3.36$), CH_4 ($\delta = 0.15$), DSS ($\delta = 0.00, 0.63, 1.75$ and 2.91) and H_2O ($\delta = 4.81$). In addition, the targeted product CH_3OH in the reaction solution was quantified via Agilent GC 7820A (using an HP-PLOT/Q column) equipped with a flame ionization detector. Gas-phase products, mainly consisting of CO, CO_2, O_2, and unreacted CH_4 were collected into an air bag to be further analyzed via gas chromatograph (GC) equipped with a Thermal Conductivity Detector.

The concentration of H_2O_2 in the reaction solution was determined via a color producing reaction of H_2O_2 and C_2KO_4Ti using a UV-1800 spectrophotometer at 387 nm. The reaction equation and detailed testing process were as follows.

$$TiO^{2+} + (H_2O_2) \rightarrow [TiO(H_2O_2)]^{2+}$$
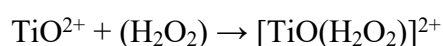
First, prepared a HA_C-NaA_C buffer solution (pH = 4.37) and a 0.1 mol/L C_2KO_4Ti chromogenic solution. Then mixed them in the ratio of buffer solution: chromogenic solution: sample solution = 3:1:1, the mixed solution would instantly turn from transparent into bright orange. Finally, stew it for 10 minutes before the test to stabilize the formed complex.

Catalyst Characterization. AC-HAADF-STEM and EDS mapping images of the samples were obtained on a Thermo Fisher Titan Themis G2 60-300 Transmission Electron Microscope. X-ray diffraction patterns (XRD) were recorded on a Rigaku SmartLab SE power X-ray diffractometer in the range of 10 °~80 ° with a step size of

0.02 °. X-ray photoelectron spectroscopy (XPS) was recorded in a Thermo Scientific Al K_α-surface analysis system. Electron Spin Resonance (ESR) Spectra of JEOL JES-FA200 ESR was employed to detect the solid state and free radicals in the reaction solution. Fourier transform infrared reflection (FT-IR) and in situ diffuse reflectance infrared Fourier transform spectroscopy (DRIFTS) was collected on a Niolet iS50 FT-IR spectrometer equipped with an MCT detector. The sample is placed in the in situ reaction chamber, with the temperature controlled by a Harrick temperature controller, and the gas flow rate is controlled by a flow meter set to 2.0 sccm. The electron paramagnetic resonance (EPR) experiments were performed with an electron spin resonance spectrometer (JES-FA 200 (JEOL)) at microwave frequencies of about 9.10 GHz on H_2O solutions in capillary tubes at ambient temperature. After the reaction, the reactor is left in the air for 5 minutes, then placed in an ice water bath to cool. Next, the solution is filtered through a filter head, transferred to a centrifuge tube, frozen with liquid nitrogen, and sent for analysis. H_2-TPR test was conducted on an AutoChem1 II 2920 instrument equipped with a TCD detector. Infeed gas was changed to 10% H_2 balanced with Ar and the profiles of H_2-TPR were recorded from 100 to 800 °C. O_2-TPD was conducted on the same instrument with a similar operating procedure as the H_2-TPR test.

The methanol yield, yield rate, and selectivity are using the following equations.

CH_3OH yield ($\mu mol \cdot g_{cat}^{-1}$) = CH_3OH Amount / Catalyst Amount,

CH_3OH yield rate ($\mu mol \cdot g_{cat}^{-1} \cdot h^{-1}$) = CH_3OH Amount / Catalyst Amount / Reaction Time,

Turnover Frequency ($mol \cdot mol_{Pd}^{-1} \cdot h^{-1}$) = CH_3OH Amount / Metal Amount / Reaction Time,

CH_3OH selectivity in aqueous phase (%) = Actual methanol yield / Products yield in liquid phase × 100%,

overall CH_3OH selectivity (%) = Actual methanol yield / Methane consumption amount × 100%.

Density functional theory (DFT) calculations. All the first-principle density functional theory (DFT) calculations were finished within the CASTEP software

package (*J Phys Condens Matter* **2002,** *14* (11), 2717-2744). For geometry optimization and phonon spectrum, we employed the generalized gradient approximation (GGA) of the Perdew-Burke-Ernzerhof (PBE) scheme (*J Chem Phys* **2013,** *138* (10); *Physical Review Letters* **1996,** *77* (18), 3865-3868; *Physic. Rev. Mat.* **2018,** *2* (12)). The energy cutoff for plane wave expansion is 570 eV. We used an energy convergence threshold of 1.0×10^{-5} eV and a force configuration tolerance of 0.03 eV/Å to obtain the optimum geometry configuration.

Section 1. Synchrotron-XAS characterizations.

The existence form of Pd and Cu elements needs to be further verified by XAS. XANES indicated that the chemical state of Pd for Cu-Pd/Anatase was close to Pd^{2+} with a similar XANES feature to that of PdO (**Figure R1a**). **Figure R1b** shows the EXAFS spectra for Pd-Cu/Anatase, Pd foil, and PdO. The Fourier-transformed (FT) k^3-weighted EXAFS spectra of Pd K-edge for Cu-Pd/Anatase in the R-space showed similar peaks to that of PdO and Pd foil in the R-space. This indicates that the catalyst surface contains both highly dispersed Pd atoms and some Pd clusters. This finding is also consistent with the Pd XPS results.
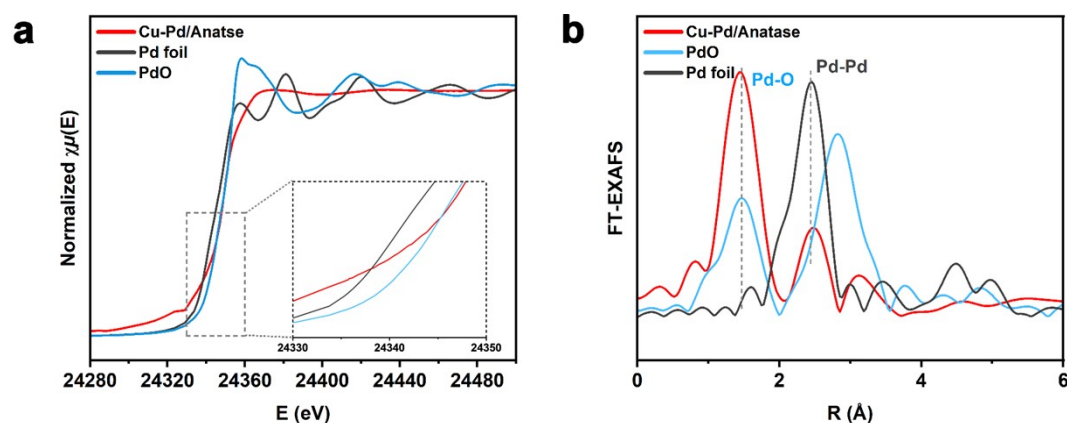

Figure R1. (a) X-ray absorption near-edge structure and (b) k^3-weighted Fourier transform spectra derived from extended X-ray absorption fine structure of Pd K edge for Cu-Pd/Anatase, Pd foil, and PdO. The data are k^3-weighted and not phase-corrected.

Wavelet transform data combined with R-space fitting information in **Figure R2** provides clear insights into the coordination environment of the sample. The wavelet analysis reveals Pd-O coordination in the first shell and Pd-Pd coordination in the second shell for the Pd species, consistent with the fitting results. This confirms the coexistence of highly dispersed atomic Pd and Pd clusters.
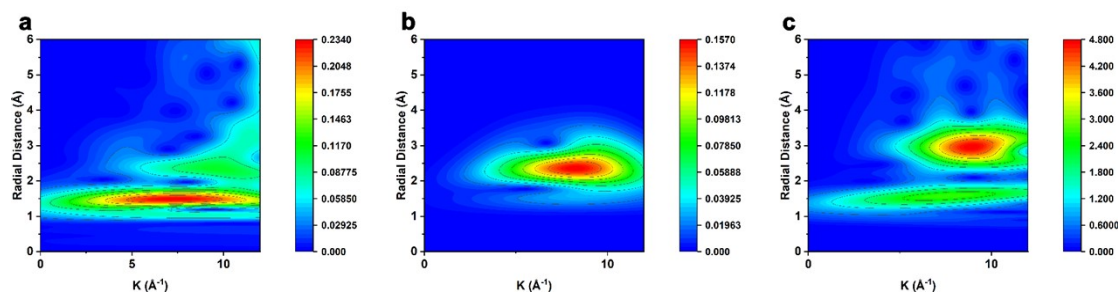

Figure R2. WT of the Pd K-edge EXAFS signals of Cu-Pd/Anatase (a), Pd foil (b), and PdO (c).

Then the coordination environment of Cu was taken into consideration. The XANES analysis indicates that the chemical state of Cu is closer to that of Cu_2O. **Figure 2d** shows the EXAFS spectra for Pd-Cu/Anatase, Cu foil, Cu2O, and CuO. The Fourier-transformed (FT) k^3-weighted EXAFS spectra of Cu K-edge showed similar peaks to that of Cu_2O and CuO in the R-space. The absence of peaks similar to those of Cu foil indicates that the Cu species primarily exist in the forms of Cu^+ and Cu^{2+}. This observation explains the Cu oxidation states observed in the Cu LMM XPS analysis and aligns with the Cu CO DRIFTS results, which suggest the presence of Cu^+.
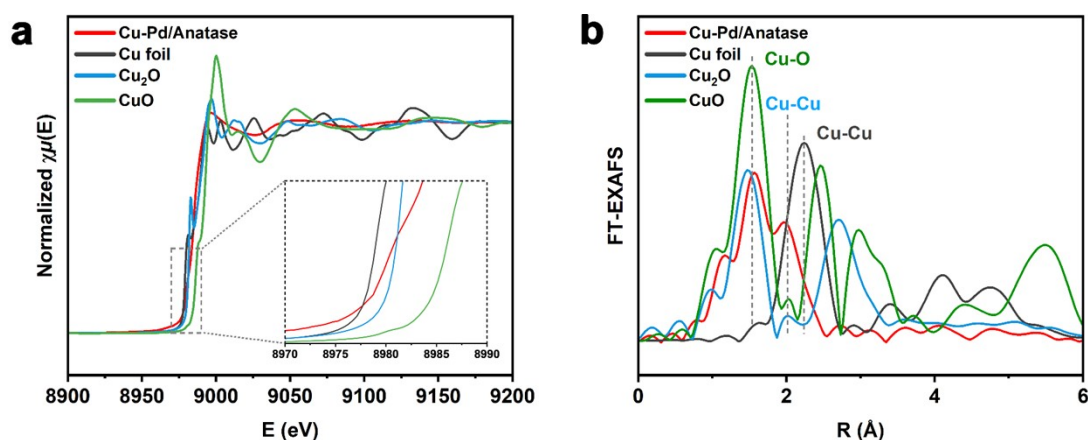

Figure R3. (a) X-ray absorption near-edge structure and (b) k^3-weighted Fourier transform spectra derived from extended X-ray absorption fine structure of Cu K edge for Cu-Pd/Anatase, Cu foil, Cu_2O, and CuO. The data are k^3-weighted and not phase-corrected.

The wavelet analysis reveals that the coordination environment of Cu in the sample is more consistent with that of Cu_2O and CuO. Additionally, Cu is observed to coordinate with Cl atoms, forming a Cu-Cl structure, which is reasonable given the confirmed presence of Cl atoms.

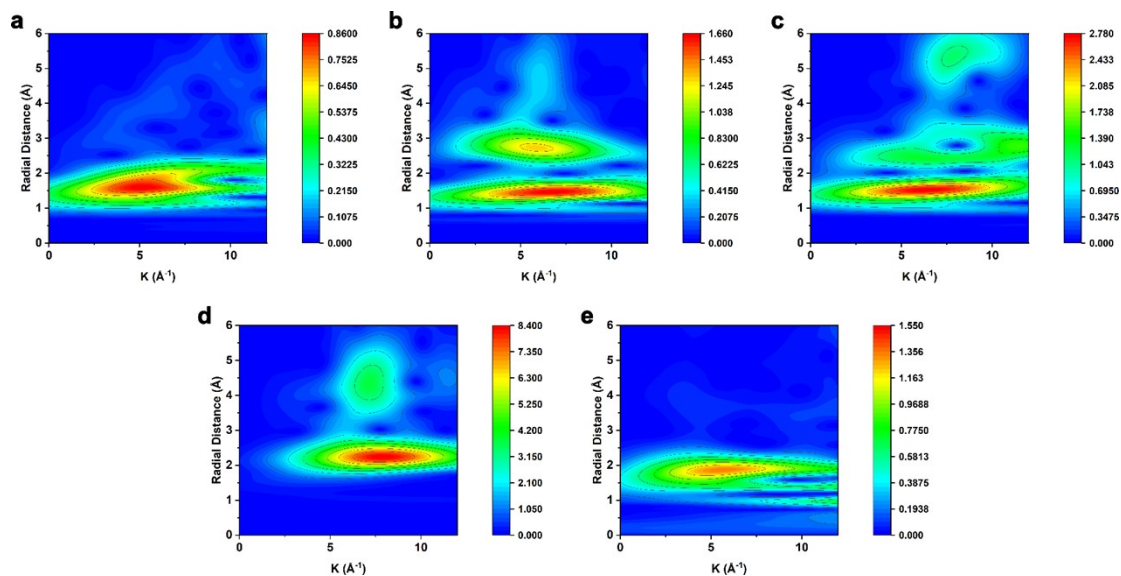The coordination environment of Cu and Pd species was fitted, and the results are summarized in **Table R1**.

Figure R4. WT of the Cu K-edge EXAFS signals of Cu-Pd/Anatase (a), Cu_2O (b), CuO (c), Cu foil (d), and CuCl (e).

Table R1. EXAFS fitting parameters at the Pd K-edge and Cu K-edge for various samples.

Sample	Path	CN^a	$R(Å)^b$	$\sigma^2(Å^2)^c$	$\Delta E_0(eV)^d$	R factor
Pd foil	Pd-Pd	12*	2.74 (±0.0018)	0.0064 (±0.0002)	-7.06 (±0.34)	0.0030
PdO	Pd-O	3.54 (±0.45)	2.02 (±0.01)	0.0013 (±0.0014)	-2.70 (±1.84)	0.0190
	Pd-Pd1	6.59 (±3.31)	3.08 (±0.02)	0.0055 (±0.0039)		
	Pd-Pd2	2.86 (±2.78)	3.46 (±0.01)	0.0005 (±0.0059)		
Cu-Pd/Anatase	Pd-O	4.69(±0.57)	2.04(±0.01)	0.0030 (±0.0014)	-4.13 (±1.77)	0.0178
	Pd-Pd	2.84 (±0.08)	2.68 (±0.02)	0.0030 (±0.0029)	-6.17 (±2.09)	0.0066
Cu foil	Cu-Cu	12.00*	2.54 (±0.00)	0.0087 (±0.0005)	4.85 (±0.56)	0.0036
Cu_2O	Cu-O1	2.03 (±0.21)	1.84 (±0.00)	0.0023 (±0.0012)	9.20 (±0.71)	0.0120
CuO	Cu-O2	4*	1.94 (±0.01)	0.0041 (±0.0012)	-1.50 (±1.36)	0.0061
Cu-Pd/Anatase	Cu-O1	4.00*	1.83 (±0.00)	0.0249 (±0.0030)	-3.39 (±1.51)	0.0115
	Cu-Cu	4.00*	2.03 (±0.01)	0.0213 (±0.0011)		
	Cu-O2	4.00*	2.33 (±0.01)	0.02828 (±0.0068)		
	Cu-Cl	0.38 (±0.04)	2.32 (±0.00)	0.0000 (±0.0000)		

^aCN, coordination number; ^bR, the distance to the neighboring atom; $^c\sigma^2$, the Mean Square

Relative Displacement (MSRD); $^d\Delta E_0$, inner potential correction; R factor indicates the goodness of the fit. $S0^2$ was fixed to 0.70-1.0, according to the experimental EXAFS fit of Rh foil by fixing CN as the known crystallographic value. * This value was fixed during EXAFS fitting, based on the known structure. Fitting range: $3.0 \leq k\ (/\text{Å}) \leq 12.4$ and $1.0 \leq R\ (\text{Å}) \leq 3.0$ (Pd foil); $3.0 \leq k\ (/\text{Å}) \leq 12.0$ and $1.0 \leq R\ (\text{Å}) \leq 3.0$ (PdO); $3.0 \leq k\ (/\text{Å}) \leq 10.0$ and $1.0 \leq R\ (\text{Å}) \leq 3.0$ (Pd Sample); $3.0 \leq k\ (/\text{Å}) \leq 12.3$ and $1.0 \leq R\ (\text{Å}) \leq 3.0$ (Cu foil); $3.0 \leq k\ (/\text{Å}) \leq 11.9$ and $1.0 \leq R\ (\text{Å}) \leq 2.0$ (Cu$_2$O); $3.0 \leq k\ (/\text{Å}) \leq 12.3$ and $1.0 \leq R\ (\text{Å}) \leq 2.0$ (CuO); $2.0 \leq k\ (/\text{Å}) \leq 12.4$ and $1.0 \leq R\ (\text{Å}) \leq 3.0$ (Cu Sample). A reasonable range of EXAFS fitting parameters: $0.700 < S_0^2 < 1.000$; $CN > 0$; $\sigma^2 > 0$ Å^2; $|\Delta E_0| < 15$ eV; R factor < 0.02.

In summary, the Pd species on the catalyst surface exist as both highly dispersed Pd atoms and as Pd clusters. The Cu species undergo charge transfer upon loading, and XAS analysis confirms that Cu exists predominantly as Cu$^+$, with no detectable Cu^0.
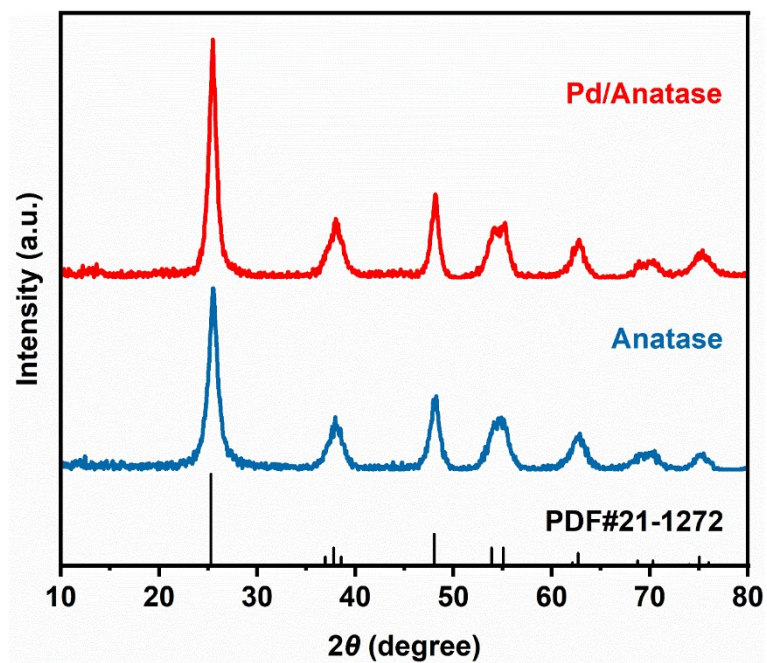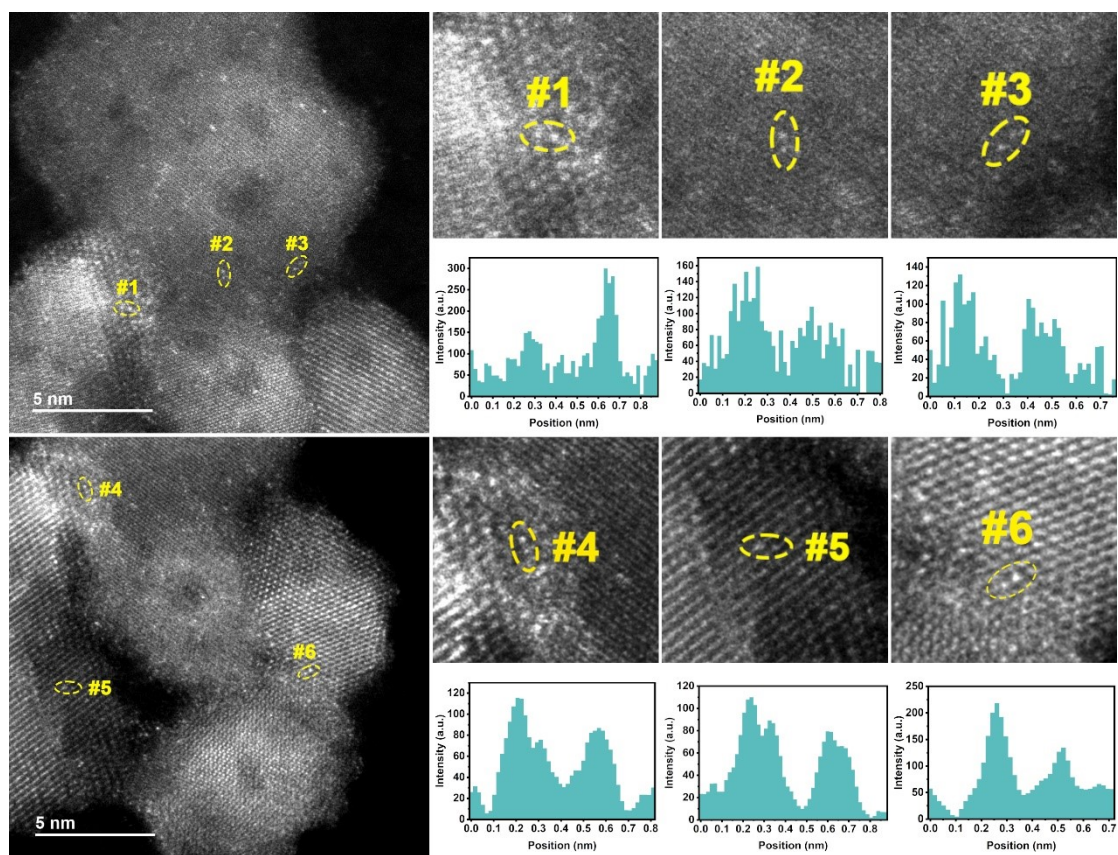
Figure S1. XRD pattern of Pd/Anatase and Anatase.

Figure S2. The AC-HAADF-STEM images of Pd/Anatase-used and the image intensity line profiles of areas in yellow circle, in which the lightest dots are Pd species and the slight light dots are Cu species.
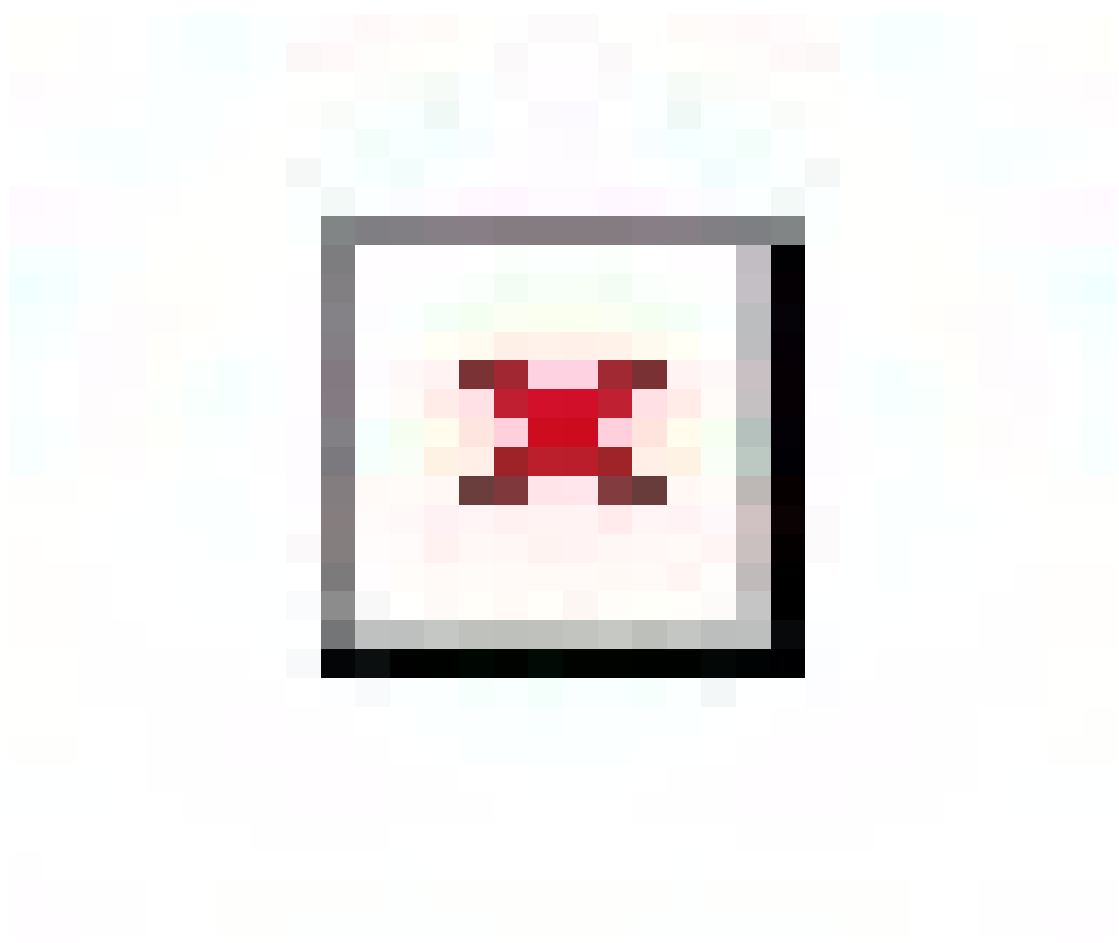
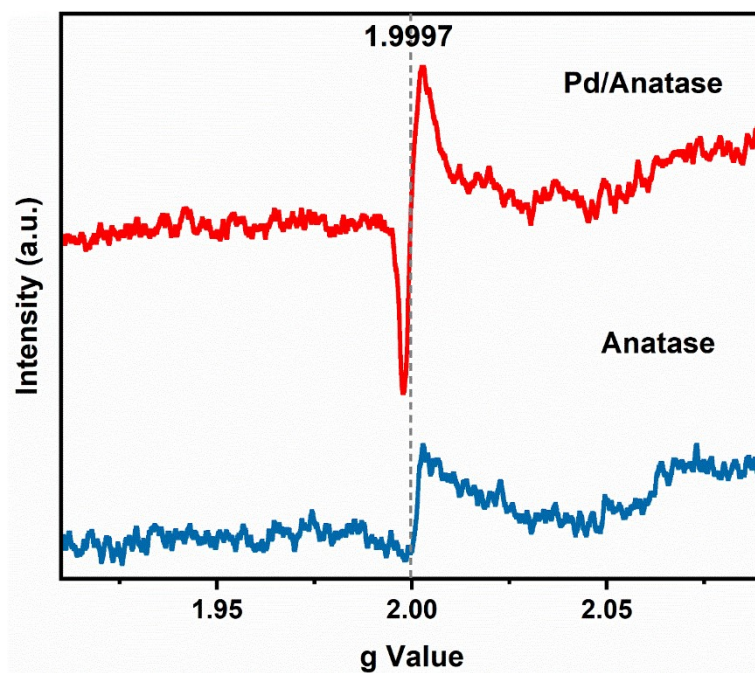**Figure S3.** The EDS mapping for Pd/Anatase-used.
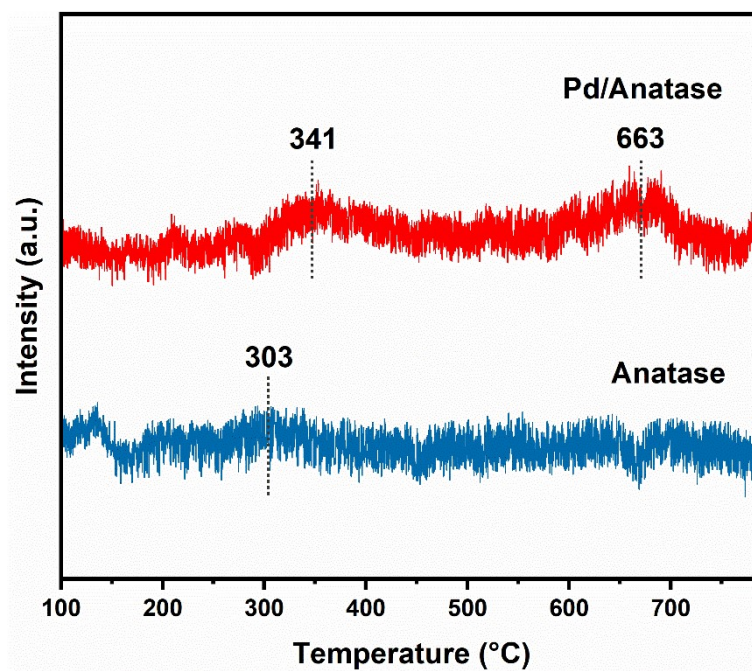
Figure S4. EPR spectra of Pd/Anatase and Anatase.

Figure S5. O$_2$ TPD profile of Pd/Anatase and Anatase.

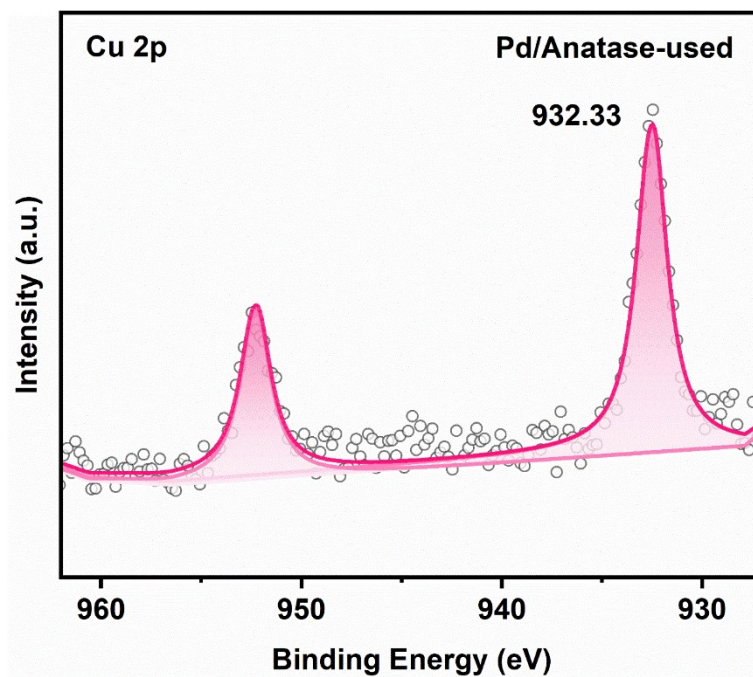The other peak at 663 °C are assigned to the subsurface oxygen and lattice oxygen desorption of the samples.

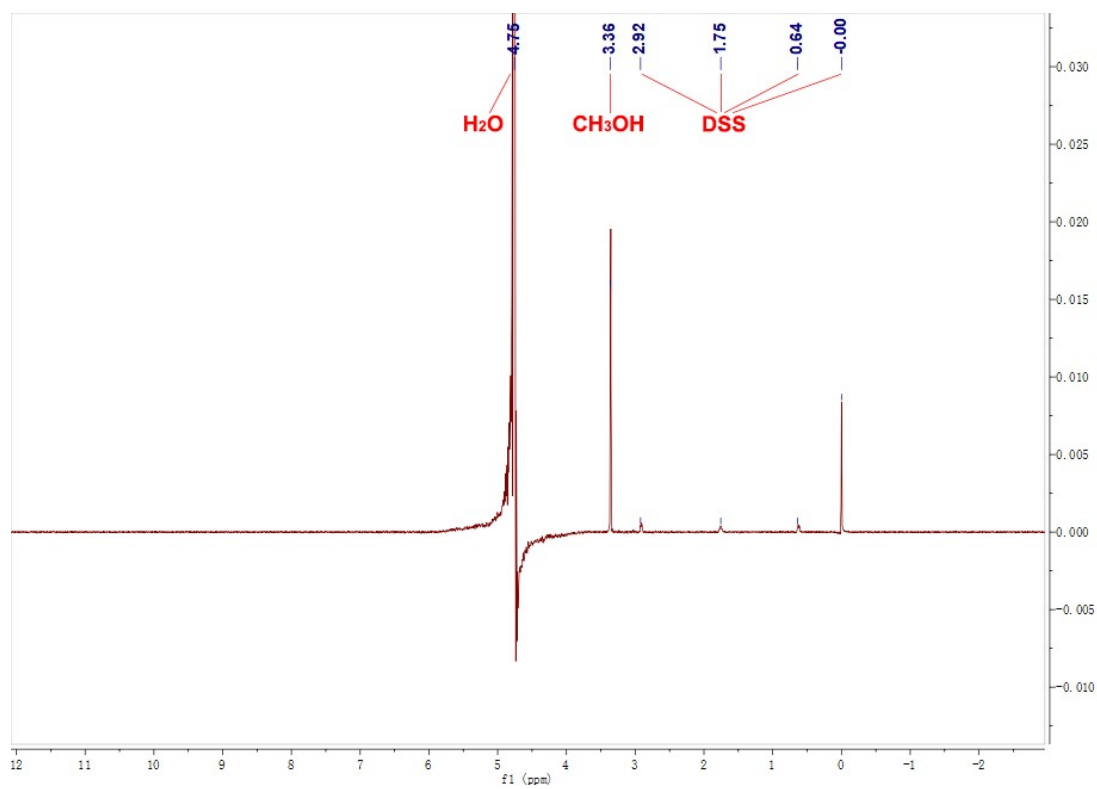**Figure S6.** Cu*2p* XPS spectra of Pd/Anatase-used.

Figure S7. ^1H NMR spectra of liquid products using Pd/Anatase with $CuCl_2$.
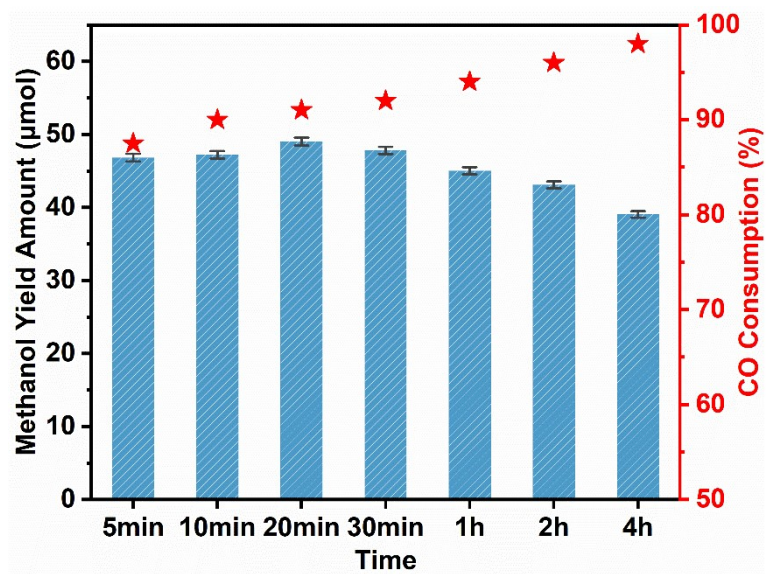
Figure S8. Effect of time over methanol yield and CO conversion.
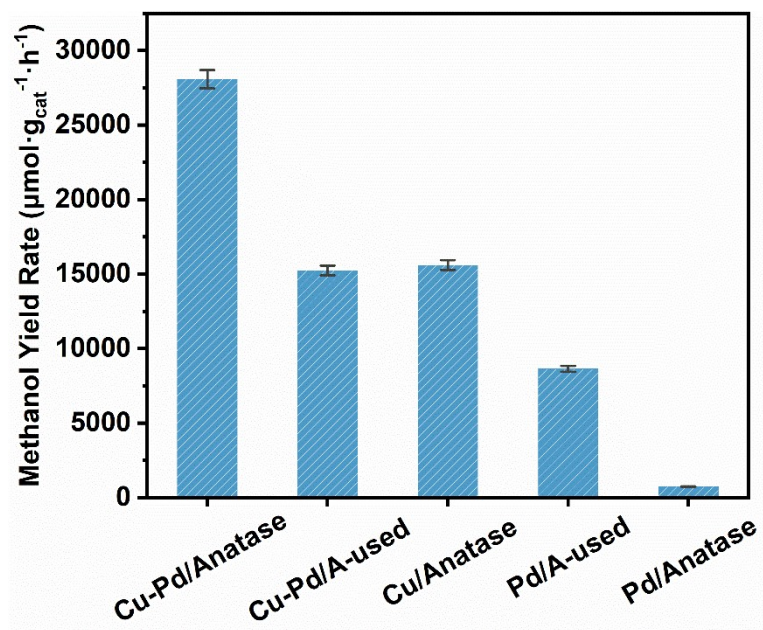
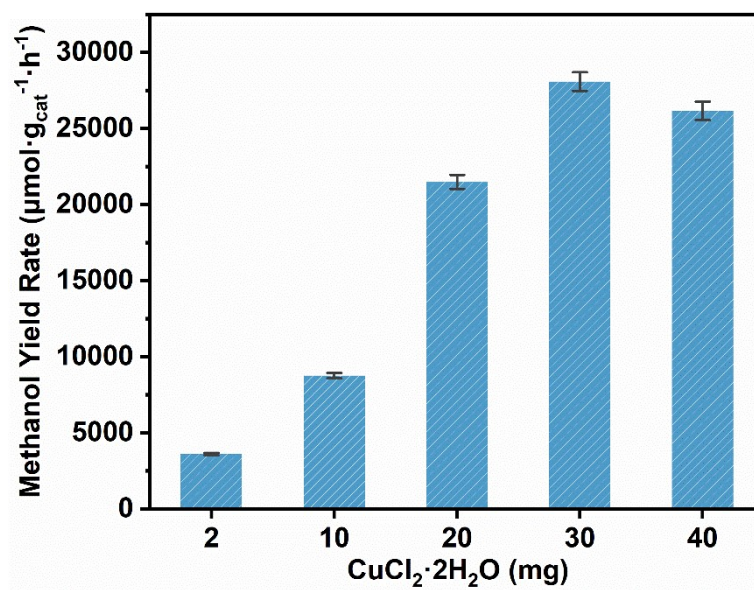**Figure S9**. Comparison between used catalysts and others.

Figure S10. Effect of CuCl$_2$ concentration on the yield of methanol.
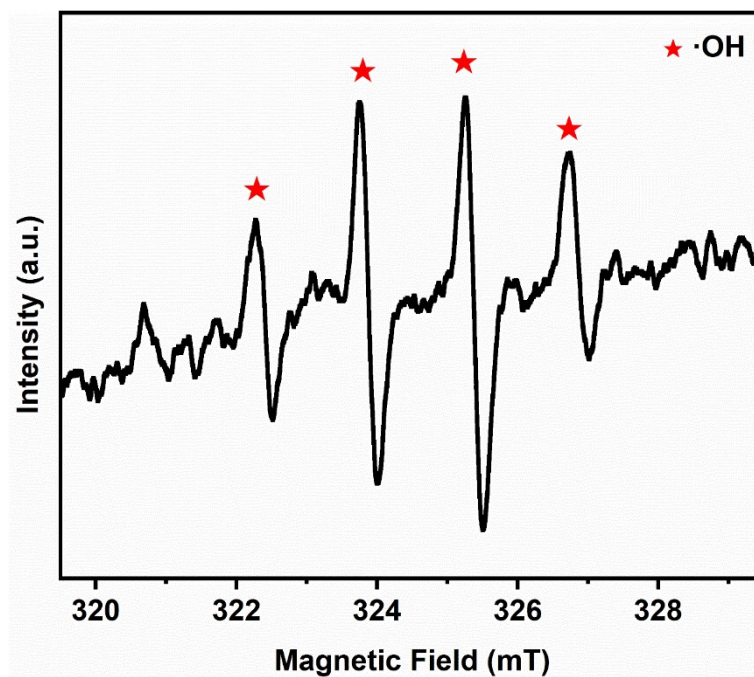
Figure S11. EPR trapping experiment with DMPO as the radical scavenger in the presence of Cu^{2+}.

The reaction condition was CH_4, O_2, CO and $CuCl_2·2H_2O$ under 150 °C.
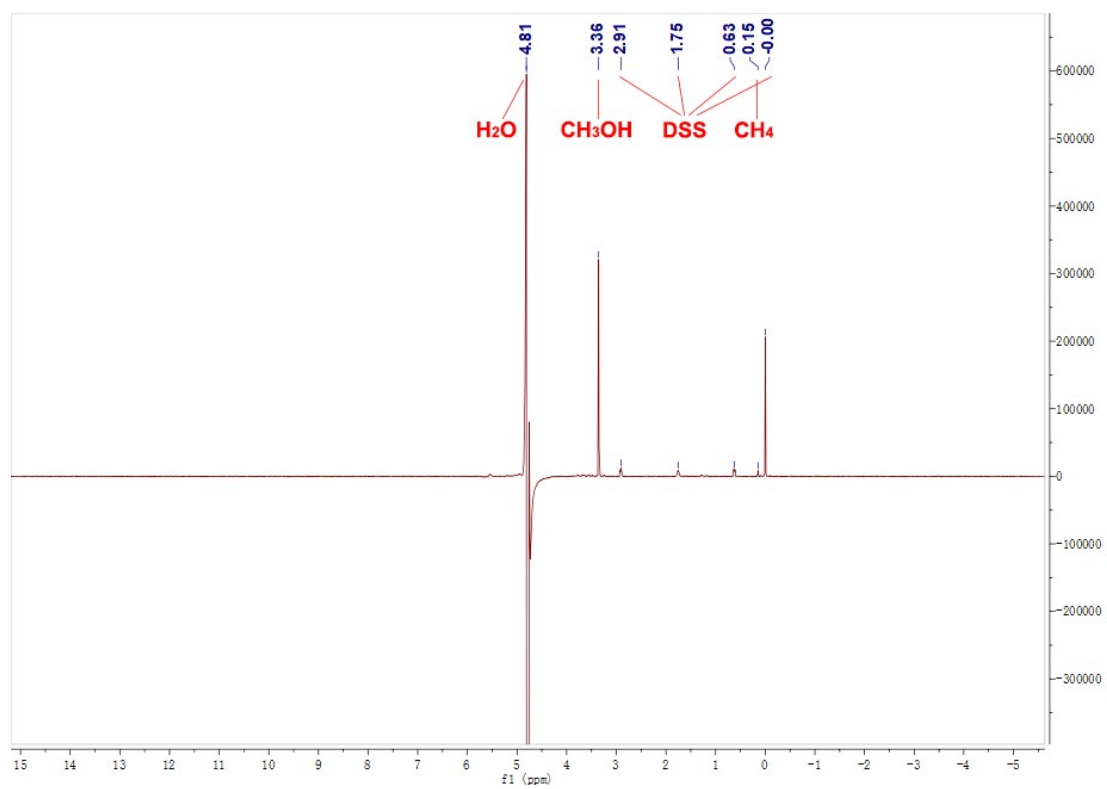
Figure S12. ^{1}H NMR spectra of liquid products using Pd/Anatase with $Cu(NO_3)_2$.
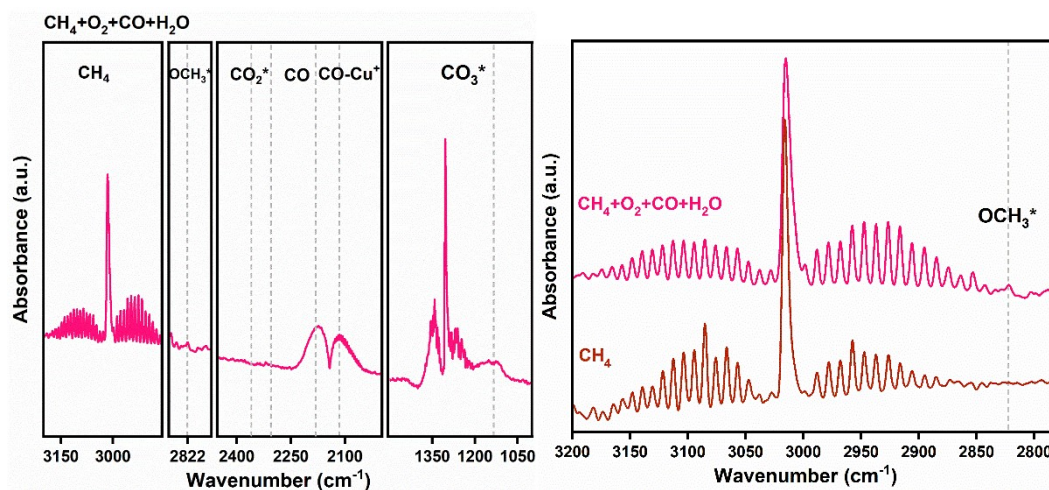
Figure S13. In situ DRIFTS spectra of reaction gas adsorption (CH_4, O_2, CO, and H_2O) at 150 °C

for $CuCl_2$. Since the intensity of OCH_3* is weak in reaction gas atmosphere (left), the comparison

between only CH_4 and reaction gas has been carried out to verify the existence of OCH_3* (right).

There is indeed a weak OCH_3* adsorption peak in the spectra of reaction gas adsorption.
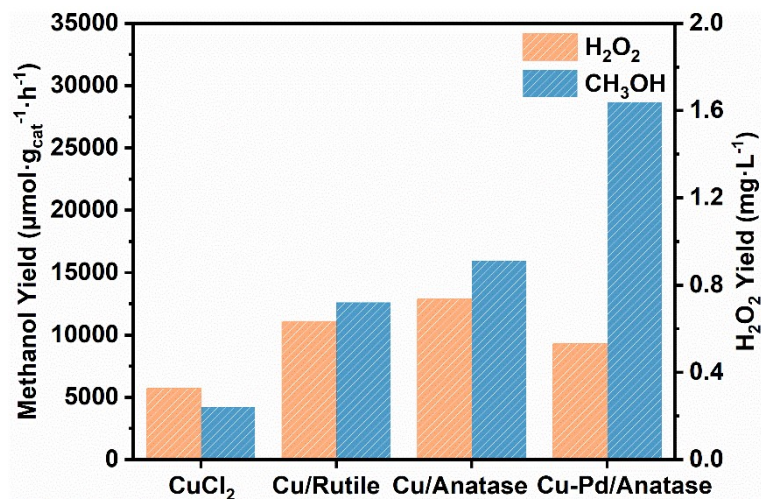
Figure S14. Effect of catalysts on the yield of methanol and H_2O_2. 20mg catalysts (Rutile, Anatase,

Pd/Anatase) were used respectively in such conditions.
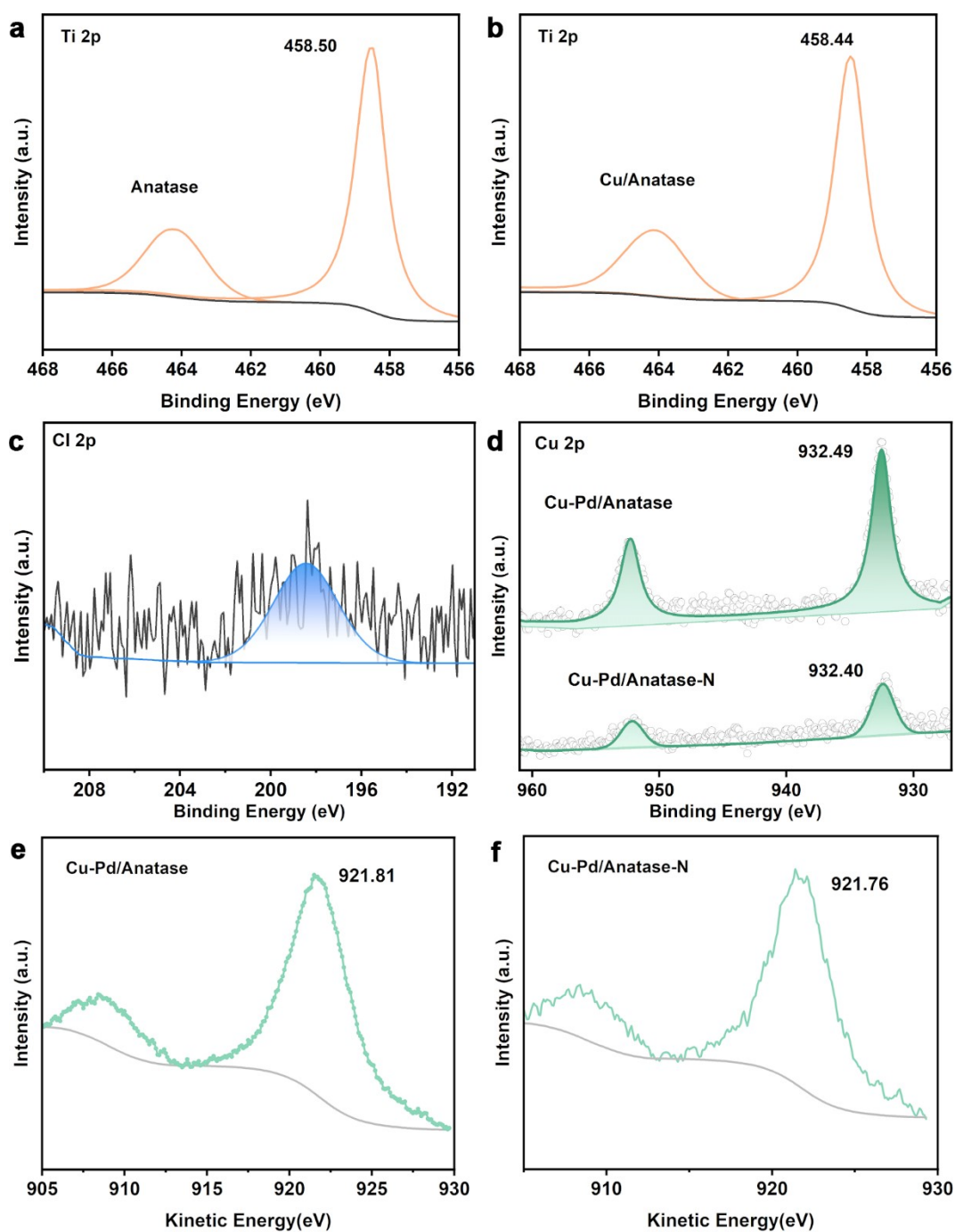
Figure S15. Ti2p XPS spectra of Anatase (a) and Cu/Anatase (b). Cu*2p* (c) and Cl*2p* (d) XPS spectra of Cu-Pd/Anatase. Cu LMM Auger spectra of Cu-Pd/Anatase (e) and Cu-Pd/Anatase-N (f).

The Cu LMM Auger spectrum is highly distinctive, showing significant charge transfer. The peaks of Cu-Pd/Anatase and Cu-Pd/Anatase-N are 921.81 eV and 921.76 eV respectively. This is markedly different from the Cu LMM positions reported in the literature, making it challenging to precisely determine the oxidation state of Cu. To

characterize the Cu oxidation state in detail, we combined Cu XAS analyses. The XANES results show that the oxidation state of Cu lies between CuO and Cu_2O. In the FT-EXAFS data, signals corresponding to CuO and Cu_2O are present, but there are no characteristic Cu-Cu peaks for Cu^0. In summary, it can be concluded that Cu^+ is present while Cu^0 is absent.
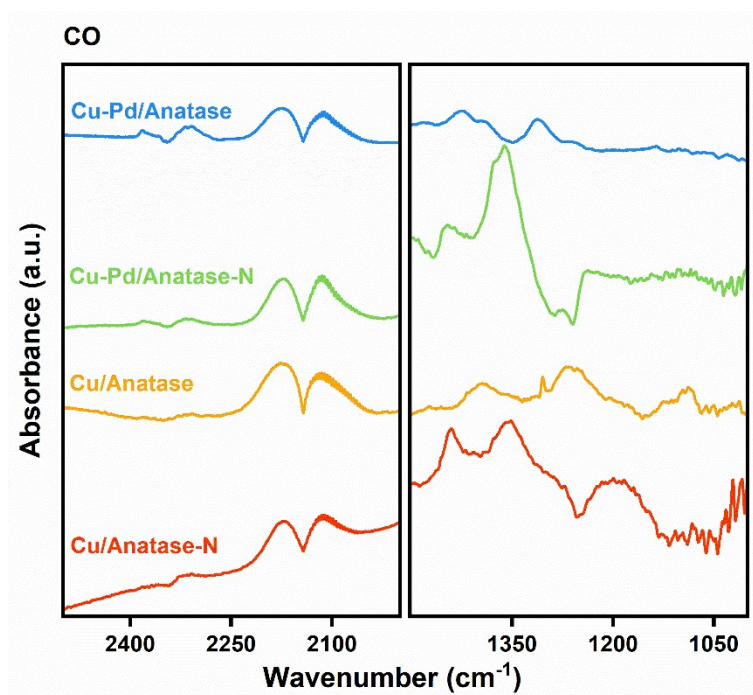
Figure S16. In situ DRIFTS of Cu/Anatase, Cu/Anatase-N, Cu-Pd/Anatase, and Cu-Pd/Anatase-N

with the introduction of CO.
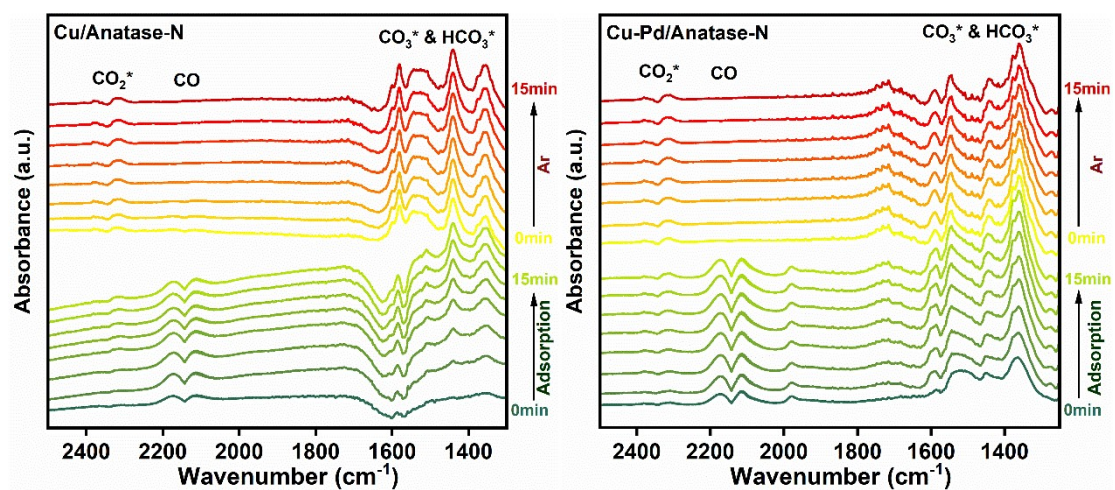
Figure S17. In situ DRIFTS spectra of Cu/Anatase-N and Cu-Pd/Anatase-N using CO probe.
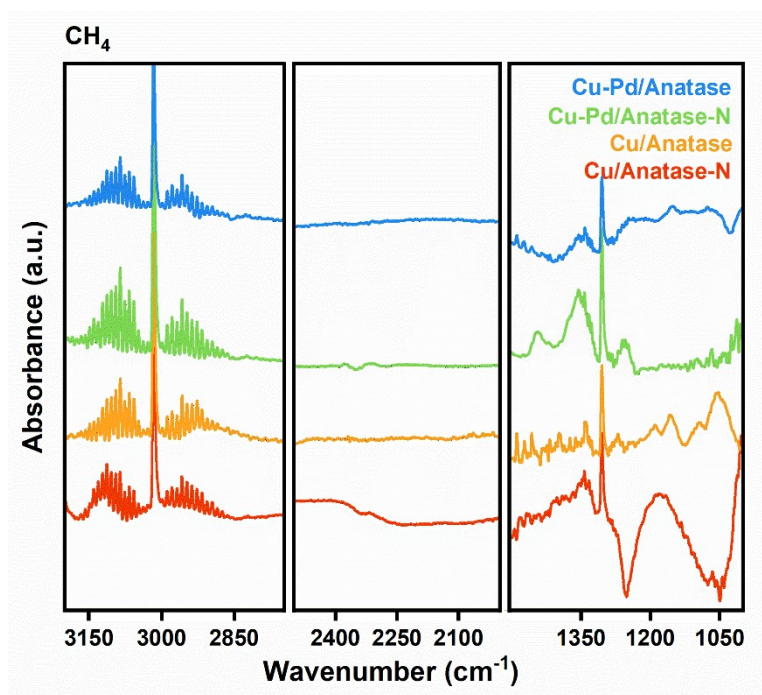
Figure S18. In situ DRIFTS of Cu/Anatase, Cu/Anatase-N, Cu-Pd/Anatase, and Cu-Pd/Anatase-N

with the introduction of CH_4.
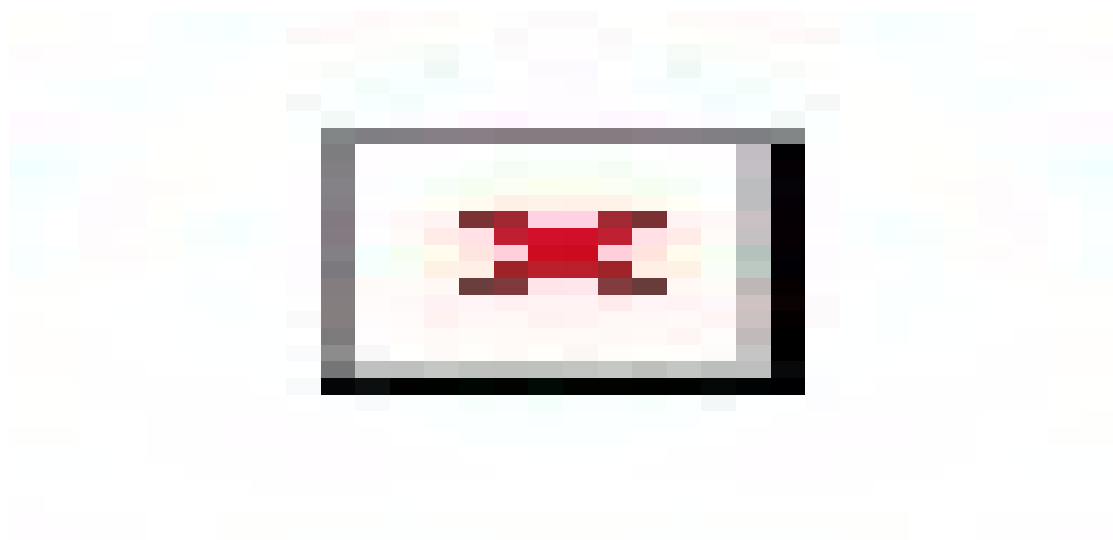
Figure S19. AC-HAADF-STEM images of (a) Pd/Anatase and (b) Pd/Anatase-used.
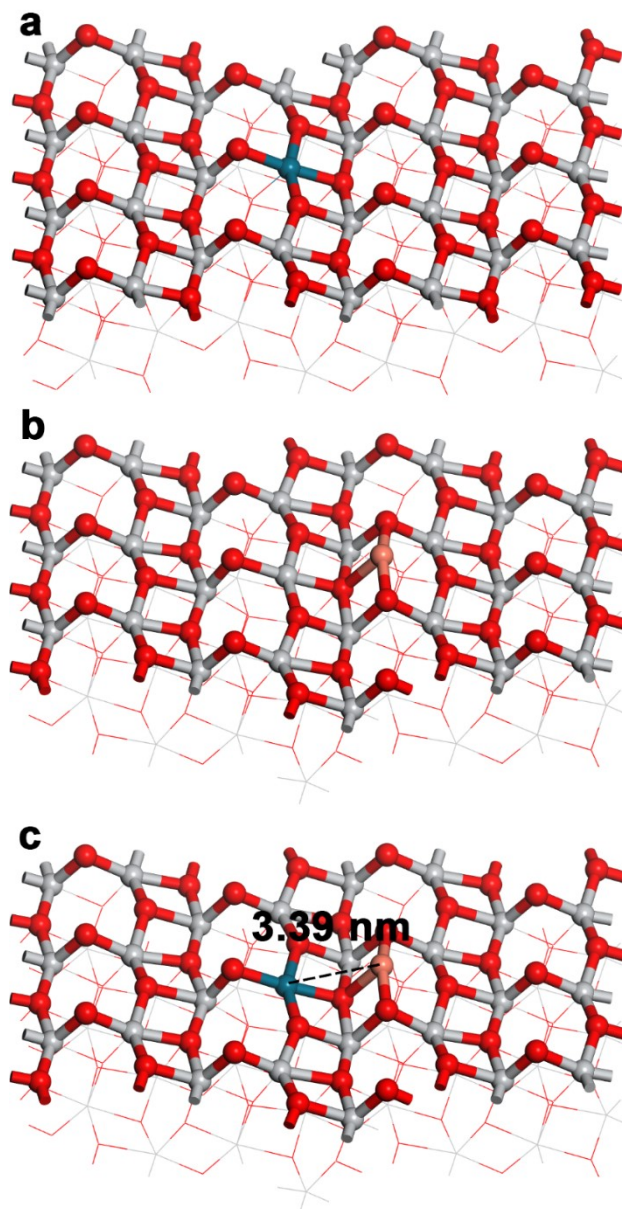
Model	Pd Mulliken Charge	Cu Mulliken Charge
Pd/Anatase	1.34	-
Cu/Anatase	-	0.56
Cu-Pd/Anatase	0.99	0.68

Figure S20. The optimized structures of (a) Pd/Anatase, (b) Cu/Anatase and (c) Cu-Pd/Anatase.

The red, grey, blue and pink spheres represent O, Ti, Pd and Cu atoms, respectively.
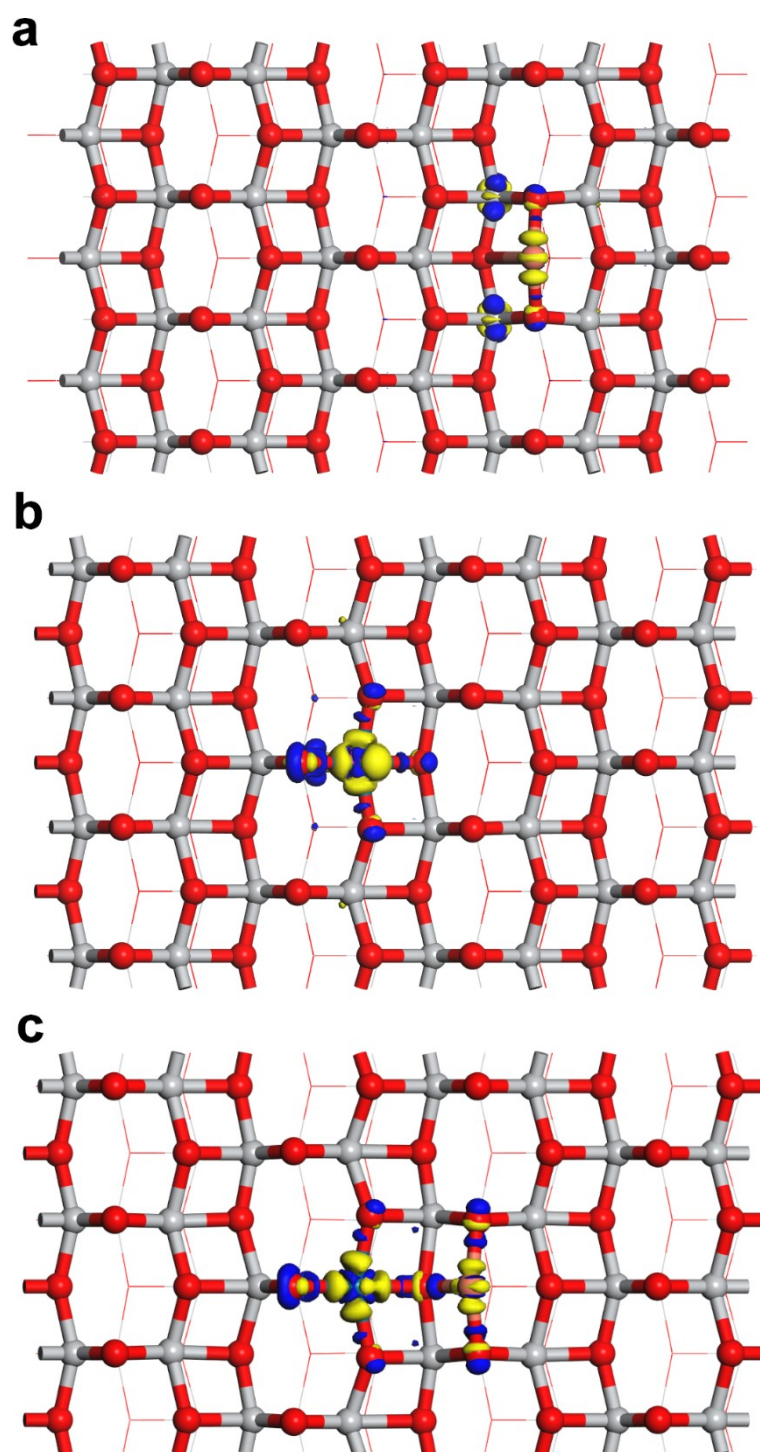
Figure S21. Calculated charge density difference (Δρ) plots of (a) Cu/Anatase, (b) Pd/Anatase and

(c) Cu-Pd/Anatase at top views, respectively. The yellow and blue area indicate an accumulation

and depletion in the electron density, respectively.
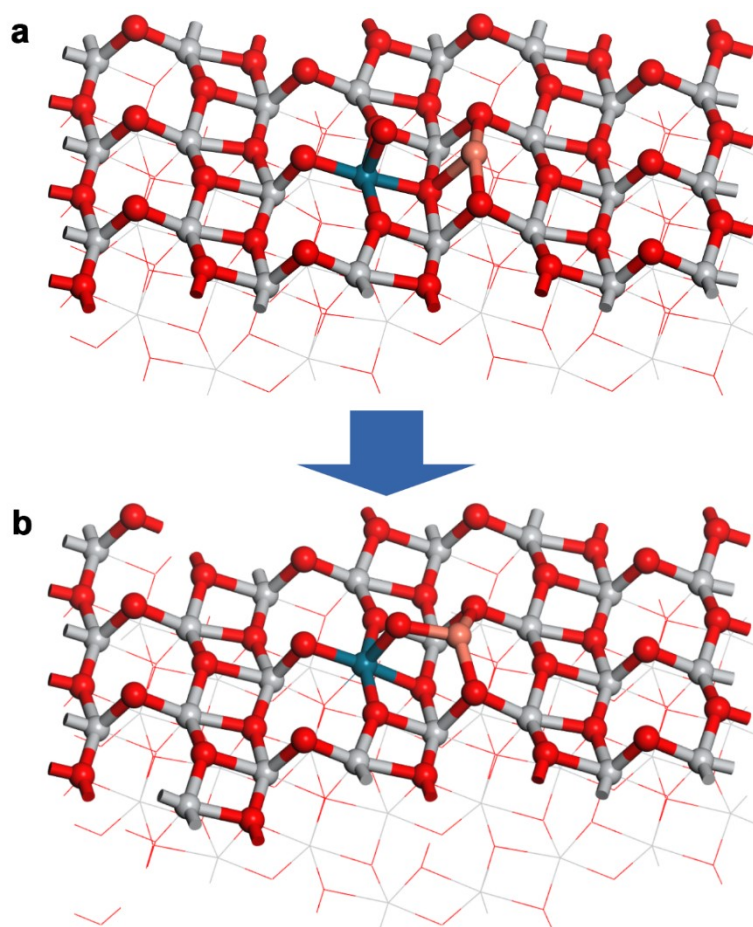
Figure S22. The initial structure (a) and optimized structure (b) of oxygen adsorption on Cu-

Pd/Anatase.
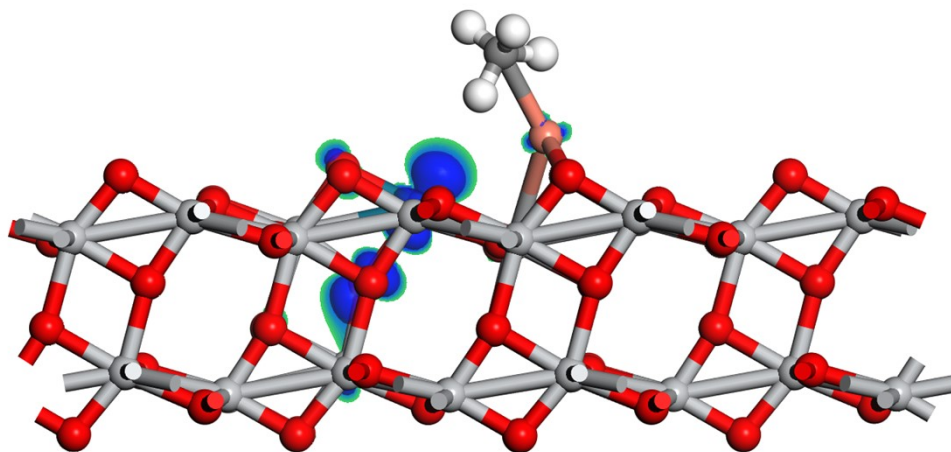
Figure S23. The spin density of *CH$_4$ adsorption on Cu-Pd/Anatase.
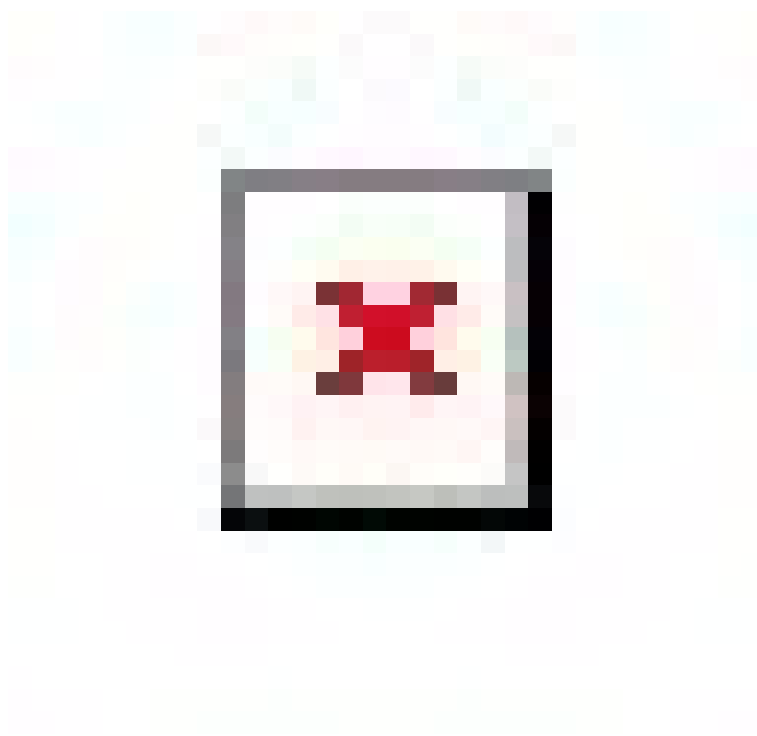
Figure S24. The C-O / M-O bond length and the H-C-H bond angle in Pd/Anatase (a), Cu/Anatase (b), and Cu-Pd/Anatase (c).
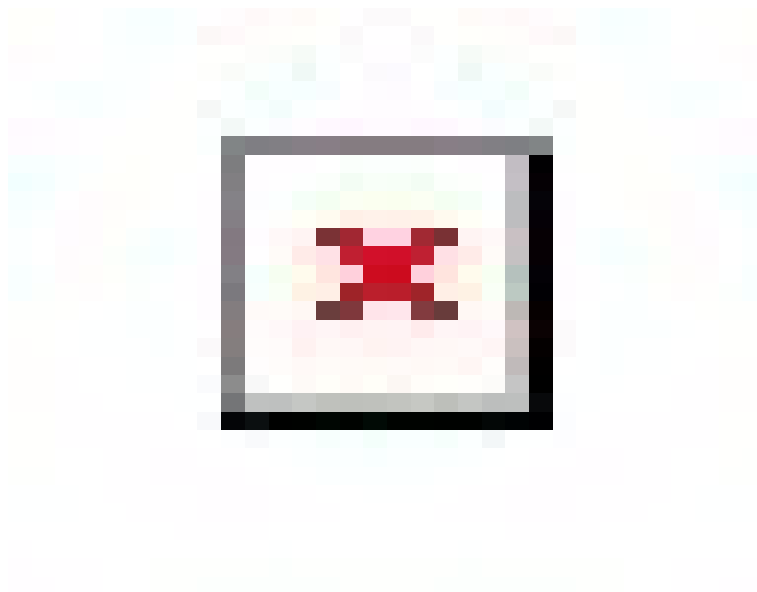
Figure S25. Projected electronic densities of states (PDOS) of 2p orbitals of CH$_3$O* on Pd/Anatase, Cu/Anatase.

Supporting Tables

Table S1. The concentration of metal in the aqueous solution.

Period	Concentration of palladium	Concentration of copper
Before reaction	-	558.717 mg·L^{-1}
After reaction	0.169 mg·L^{-1}	0.010 mg·L^{-1}
After washing	0.216 mg·L^{-1}	3.254 mg·L^{-1}

Although Pd leaches out after the reaction, its loss relative to the total Pd is minimal. We have already demonstrated in Figure 2b that the main active sites are not only Pd atoms, so the cyclic nature shown in Figure 2c can still be maintained.

Table S2. The comparison of selective methane oxidation performance over Cu-Pd/Anatase and other reported catalysts.

Catalyst	Reaction condition		Product ($\mu mol \cdot g_{cat}^{-1} \cdot h^{-1}$)				CH$_3$OH selectivity (%)	Ref.
	Reactants	Temperature (°C)	CH$_3$OH	CH$_3$OOH	HCOOH	CH$_3$COOH		
Cu-Pd /Anatase	2.0 MPa CH$_4$; 0.3 MPa O$_2$; 0.5 MPa CO; 20 mL H$_2$O; 20 mg Cat.; 30mg CuCl$_2$·2H$_2$O	150	28080	-	-	-	>99	This work
0.5 Rh/TiO$_2$	2.3 MPa CH$_4$; 0.3 MPa O$_2$; 0.5 MPa CO; 20 mL H$_2$O; 16 mg Cat.; 40mg CuCl$_2$	150	2629	-	-	-	>99	1
Au/H-MOR	2.0 MPa CH$_4$; 0.5MPa O$_2$; 0.5 MPa CO; 20 mL H$_2$O; 100 mg Cat.	150	1296	26	9	46	75	2
IrCuPd-ZSM-5	2.0 MPa CH$_4$; 0.4 MPa O$_2$; 0.5 MPa CO; 20 mL H$_2$O; 40 mg Cat.	150	1188	-	0	81	~80	3
PdCu/ZSM-5	2.4 MPa CH$_4$; 0.3 MPa O$_2$; 0.8 MPa H$_2$; 20 mL H$_2$O; 30 mg Cat.	120	707	11	460	-	~60	4
AuPd@ZSM-5-C$_{16}$	3.0 MPa with 3.3% H$_2$/6.6% O$_2$/1.6% CH$_4$/61.7% Ar/26.8% He; 10 mL H$_2$O; 27mg Cat.	70	64.1[a]	-	3.6[a]	-	92	5
Pd/CsPMA	2.0 MPa CH$_4$; 0.3 MPa O$_2$; 0.4 MPa H$_2$; 2 mL D$_2$O; 10 mg Cat.	Room temperature	67.4 [b]	-	-	-	100	6
Au-ZSM-5	2.07 MPa CH$_4$; 0.42 MPa air; 15 mL H$_2$O; 100mg Cat.	240	66.48	1.70	-	1.74	48	7

a: μmol, 30 min;

b: Step 1: H$_2$ 15min; Step 2: CH$_4$ + O$_2$ 5min.

Table S3. H_2O_2 yields under typical reaction conditions.

Entry	CO (bar)	O_2 (bar)	Catalyst	Cu^{2+} source	H_2O_2 (mg·L^{-1})
1	5	0	-	$CuCl_2$	0
2	5	3	-	$CuCl_2$	0.326
3	0	3	-	$CuCl_2$	0
4	5	3	Anatase	$CuCl_2$	0.735
5	5	3	Pd/Anatase	$CuCl_2$	0.530
6	5	3	Anatase	-	0
7	5	3	Pd/Anatase	-	0
8	5	3	-	$Cu(NO_3)_2$	0.155
9	5	3	Pd/Anatase	$Cu(NO_3)_2$	0.314
10	5	3	Pd/Anatase	$Cu(NO_3)_2$ + 10 mg NaCl	0.360
11	5	3	Pd/Anatase	$Cu(NO_3)_2$ + 20 mg NaCl	0.531
12	5	3	Pd/Anatase	$Cu(NO_3)_2$ + 40 mg NaCl	0.530

30 mg $CuCl_2·2H_2O$ and 25.4 mg $Cu(NO_3)_2·3H_2O$ are used respectively to ensure the same amount of copper ions.

Table S4. The effects of reactant composition on the yield of methanol. Typical reaction conditions: 20 mg catalysts and 30 mg $CuCl_2 \cdot 2H_2O$ are dispersed in 20 mL water, and the reaction time is 5 min.

Entry	CH_4 (bar)	CO (bar)	O_2 (bar)	H_2O_2 (mol·L^{-1})	CH_3OH Yield (μmol·g$_{cat}$$^{-1}$·h^{-1})
1	20	5	3	0	28080
2	20	5	0	0	0
3	20	0	3	0	1656
4	20	0	0	0	0
5	20	0	0	0.5	5414
6	20	5	0	0.5	35519

Table S5. The effects of anions on the yield of methanol. Typical reaction conditions: 20mg catalysts, 2.0 MPa CH_4, 0.5 MPa CO and 0.3 MPa O_2, 150 °C and 5 min (entries 1-9). Methane oxidation with H_2O_2: 20 mg catalysts, 2.0 MPa CH_4, 0.5 MPa CO and 0.5 M H_2O_2 (entries 10 and 11).

Entry	Catalyst	Reaction condition		CH_3OH ($\mu mol \cdot g_{cat}^{-1} \cdot h^{-1}$)
		Cu^{2+} source	Oxidant	
1	-	$CuCl_2$	O_2/CO	4206
2	-	$Cu(NO_3)_2$	O_2/CO	1632
3	Pd/Anatase	$CuCl_2$	O_2/CO	28080
4	Pd/Anatase	$Cu(NO_3)_2$	O_2/CO	16596
5	Pd/Anatase	$Cu(NO_3)_2$ + 10 mg NaCl	O_2/CO	20977
6	Pd/Anatase	$Cu(NO_3)_2$ + 20 mg NaCl	O_2/CO	25211
7	Pd/Anatase	$Cu(NO_3)_2$ + 40 mg NaCl	O_2/CO	23715
8	Pd/Anatase	NaCl	O_2/CO	0
9	Pd/Anatase	$CuCl_2$	H_2O_2	35519
10	Pd/Anatase	$Cu(NO_3)_2$	H_2O_2	23112

Table S6. The effects of anions on the reaction gas. Typical reaction conditions: 20 mg Pd/Anatase, 2.0 MPa CH_4, 0.5 MPa CO and 0.3 MPa O_2, 150 °C and 5 min.

Entry	Cu^{2+} source	CO Concentration (%)	selectivity of CH_4 to CH_3OH (%)
1	$CuCl_2$	87.5	86.7
2	$Cu(NO_3)_2$	22.0	44.6

Table S7. The CO adsorption amount with different Cu^{2+} sources.

Entry	Cu^{2+} source	CO Adsorption Amount (cc/g)
1	$CuCl_2$	7.5236
2	$Cu(NO_3)_2$	0.5932

Table S8. C-O / M-C bond length and H-C-H bond angle in different adsorbed methane structures.

	C-M / C-O bond length (Å)	H-C-H bond angle (°)
Pd/Anatase	1.383	106.202
Cu/Anatase	1.424	109.006
Cu-Pd/Anatase	1.939	112.883
Pd/Anatase with Cl	1.398	107.001
Cu/Anatase with Cl	1.425	109.066
Cu-Pd/Anatase with Cl	1.893	108.809

Table S9. The effect of Cl on the Mulliken charge of Cu in Cu-Pd/Anatase.

	Cu Mulliken Charge
Cu-Pd/Anatase	0.68
Cu-Pd/Anatase with Cl	0.55

Table S10. The influence of Cl on the adsorption energy of CO.

	CO adsorption Energy (eV)
Cu-Pd/Anatase	0.65
Cu-Pd/Anatase with Cl	-1.02

Table S11. The energy for the cleavage of H_2O_2.

	H_2O_2 Decomposition Product	Energy (eV)
Cu-Pd/Anatase	*OH + *OH	-3.23
	*H + *OOH	-1.03
Cu-Pd/Anatase with Cl	*OH + *OH	-1.23
	*H + *OOH	-0.37

References

1.	Gu, F.; Qin, X.; Li, M.; Xu, Y.; Hong, S.; Ouyang, M.; Giannakakis, G.; Cao, S.; Peng, M.; Xie, J.; Wang, M.; Han, D.; Xiao, D.; Wang, X.; Wang, Z.; Ma, D., Selective Catalytic Oxidation of Methane to Methanol in Aqueous Medium over Copper Cations Promoted by Atomically Dispersed Rhodium on TiO$_2$. *Angewandte Chemie International Edition* **2022,** *61* (18), e202201540.

2.	Wang, W.; Zhou, W.; Tang, Y.; Cao, W.; Docherty, S. R.; Wu, F.; Cheng, K.; Zhang, Q.; Copéret, C.; Wang, Y., Selective Oxidation of Methane to Methanol over Au/H-MOR. *Journal of the American Chemical Society* **2023,** *145* (23), 12928–12934.

3.	Li, M.; Shan, J.; Giannakakis, G.; Ouyang, M.; Cao, S.; Lee, S.; Allard, L. F.; Flytzani-Stephanopoulos, M., Single-step selective oxidation of methane to methanol in the aqueous phase on iridium-based catalysts. *Applied Catalysis B: Environmental* **2021,** *292*, 120124.

4.	Wu, B.; Lin, T.; Huang, M.; Li, S.; Li, J.; Yu, X.; Yang, R.; Sun, F.; Jiang, Z.; Sun, Y.; Zhong, L., Tandem Catalysis for Selective Oxidation of Methane to Oxygenates Using Oxygen over PdCu/Zeolite. *Angewandte Chemie International Edition* **2022,** *61* (24), e202204116.

5.	Jin, Z.; Wang, L.; Zuidema, E.; Mondal, K.; Zhang, M.; Zhang, J.; Wang, C.; Meng, X.; Yang, H.; Mesters, C.; Xiao, F.-S., Hydrophobic zeolite modification for in situ peroxide formation in methane oxidation to methanol. *Science* **2020,** *367* (6474), 193-197.

6.	Wang, S.; Fung, V.; Hülsey, M. J.; Liang, X.; Yu, Z.; Chang, J.; Folli, A.; Lewis, R. J.; Hutchings, G. J.; He, Q.; Yan, N., H2-reduced phosphomolybdate promotes room-temperature aerobic oxidation of methane to methanol. *Nature Catalysis* **2023,** *6*, 895–905.

7.	Qi, G.; Davies, T. E.; Nasrallah, A.; Sainna, M. A.; Howe, A. G. R.; Lewis, R. J.; Quesne, M.; Catlow, C. R. A.; Willock, D. J.; He, Q.; Bethell, D.; Howard, M. J.; Murrer, B. A.; Harrison, B.; Kiely, C. J.; Zhao, X.; Deng, F.; Xu, J.; Hutchings, G. J., Au-ZSM-5 catalyses the selective oxidation of CH$_4$ to CH$_3$OH and CH$_3$COOH using O$_2$. *Nature Catalysis* **2022,** *5* (1), 45-54.